


Measurement of internal dark current in a 17 GHz accelerator structure with an elliptical sidewall

Haoran Xu¹,* Michael A. Shapiro, and Richard J. Temkin

Massachusetts Institute of Technology, Cambridge, Massachusetts 02139, USA

 (Received 28 January 2020; accepted 13 March 2020; published 26 March 2020)

A 17 GHz single cell, standing wave, copper accelerator structure with an axisymmetric elliptical central cell sidewall was tested for internal and downstream dark current as a function of gradient up to 93 MV/m. The elliptical sidewall was predicted to suppress the internal dark current and the lower order multipactor modes as compared with a previously tested structure having a straight sidewall. During the conditioning phase of the elliptical sidewall structure, strong internal dark current generated by an $N = 1$ multipactor mode was observed at gradients in the 10 to 20 MV/m range. After conditioning with 2.2×10^5 pulses to 93 MV/m, the $N = 1$ mode was completely suppressed and no multipactor resonances were observed. The internal dark current was reduced to a comparatively low level, much smaller than in the previously studied, straight sidewall structure, in good agreement with simulations. The energy spectrum of the electrons colliding with the sidewall was measured using an isolated side dark current monitor and a bias voltage. As the conditioning progressed, the electron energy spectrum showed an increase in the concentration of lower energy electrons, also in good agreement with simulations. Studies of internal dark current may help to understand the rf conditioning and ultimate performance of high gradient accelerator structures.

DOI: [10.1103/PhysRevAccelBeams.23.031003](https://doi.org/10.1103/PhysRevAccelBeams.23.031003)

I. INTRODUCTION

Internal dark current is the part of the dark current generated inside an accelerator structure that terminates within the structure itself, as opposed to the upstream or downstream dark current that propagates out of the structure. Simulations have shown that the fraction of the total dark current, presumably generated by field emission, that can make it all the way along the beam axis and be received by the Faraday cups at the ends of the accelerator structure is very tiny [1–3]. Although there have been many studies of the upstream and downstream dark current, a thorough investigation on the effect of the interaction of the internal dark current with the accelerator structure is also of great importance. Vacuum microwave breakdown poses a major research challenge in the study of high gradient accelerators. A breakdown causes the loss of the established accelerating field inside an accelerator, the reflection of the incident microwave power and possible damage to the accelerator inner surfaces. A better understanding of the internal dark current will contribute to the study of the breakdown problem in normal conducting rf accelerator structures.

*haoranxu@mit.edu

Published by the American Physical Society under the terms of the Creative Commons Attribution 4.0 International license. Further distribution of this work must maintain attribution to the author(s) and the published article's title, journal citation, and DOI.

Among the various physical phenomena induced by the interception of internal dark current with the accelerator structure inner surfaces, secondary electron emission (SEE) is of our primary interest. At high gradient, e.g., above 80 MV/m at 17 GHz, the dark current electrons generated by field emission always carry 10^2 keV energy upon collision, and the corresponding secondary electron yield (SEY) is much lower than unity. On the accelerator inner surfaces where the electric field is intense, this dark current interception is unlikely to cause an electron multipactor instability, because the secondary electrons will in turn gain so much energy that their SEY of collision is still far less than one, rendering the secondary electron emission process convergent. On the surfaces where the electric field is weak, however, the secondary electrons cannot gain enough energy between collisions to constrain their SEY to below unity. They witness a certain amount of acceleration by local radial and axial electric fields between collisions, and, with an SEY greater than one, they can generate more electrons upon collision [4,5]. When the resonant conditions are met, a multipactor discharge of electrons is formed. During the development stage of the multipactor, the number of electrons witnesses an exponential growth until a state of saturation is reached, when the space-charge force from the electron cloud suppresses further increase of the electron population. This multipactor electron cloud internal dark current interaction with the accelerator surface can be very significant [5].

In our prior study of the internal dark current at 17 GHz, several multipactor modes were identified on the sidewall of the central cell of a standing wave single cell disk-loaded waveguide (DLWG) structure under high gradient operation [5]. This structure had an axisymmetric straight central cell sidewall and we designate it as the S structure in this paper.

We found that the multipactor current on the sidewall of the accelerator structure was estimated to be $\sim 15\text{--}30$ A over the acceleration gradient range of 80–90 MV/m. This intense interaction of 10^2 eV electrons with a metal surface can easily give rise to outgassing [6–9], gas ionization [10,11], and photon emission in the ultraviolet band and beyond [12–14], which can all contribute to the instability of the high gradient accelerator operation. In order to reduce, and even eliminate the multipactor on the accelerator cell sidewall, our first effort went to changing the material surface SEY curve by the applications of coatings of diamondlike carbon and titanium nitride (TiN), which had been known to display relatively low SEY values over the incident electron energy range concerned [15,16]. The high gradient experimental results showed modest improvement in reducing the internal dark current [5].

To better suppress the multipactor modes, our next effort was on making geometrical changes on the accelerator cell sidewall so that the multipactor resonant conditions could no longer hold [17–20]. In this regard, a 17 GHz single cell standing wave accelerator structure with an axisymmetric elliptical central cell was fabricated and tested under high power at MIT. The results are presented in this paper. This elliptical sidewall structure is denoted as the E structure.

Prior studies on single surface multipactor instabilities mainly focused on superconducting accelerator designs at lower operating frequencies in L-band and S-band, and at lower gradients [21–24]. For a high gradient room temperature accelerator structure operating at 17 GHz, the operating regime is quite different. At SLAC, internal dark current probes were installed along the equators in an S-band normal conducting accelerator structure for internal field emission dark current detection and azimuthal symmetry check [25,26]. In another experimental effort at SLAC, high gradient tests of a copper accelerator structure operating at X-band at a cryogenic temperature of 40 K reported that the dark current loading was one possible limiting factor on achieving higher gradients [27,28]. A recent theoretical study at CERN on a traveling wave CLIC prototype accelerator structure indicated that multipactor modes were observed in the particle-in-cell (PIC) simulations for an operating gradient of 100 MV/m [29].

In this paper, the experimental setup for the high gradient test is introduced in Sec. II. Section III describes the design of the above-mentioned standing wave structure with an axisymmetric elliptical central cell sidewall. Section IV is on the dark current PIC and particle tracking simulations of the structure. The design and simulation of the

experimental accelerator structure are covered in Sec. V. The fabrication of the experimental accelerator structure is described in Sec. VI, followed by Sec. VII that reports the experimental results. Finally, the discussion of the experimental results and the conclusions are made in Sec. VIII.

II. EXPERIMENTAL SETUP

Figure 1 shows the diagram of the experimental setup for testing of the 17 GHz accelerator structures at high gradient. The 17 GHz input analog signal is shaped into a square pulse, amplified by the solid state amplifier, and transmitted to a traveling wave relativistic klystron produced by Haimson Research Corporation [30]. The klystron operates at a center frequency of 17.145 GHz, has a bandwidth of 20 MHz, and can generate 10–1000 ns pulses with an output power up to 25 MW at 76 dB gain. A 4.4 dB hybrid is used after the klystron to protect it from the rf power reflection due to frequency mismatch or breakdowns in the accelerator structure under test. The vacuum of the chamber in which the accelerator structure is installed and the klystron vacuum are separated by a ceramic window.

In the experiment, the oscilloscope traces of the forward rf power signal, the downstream dark current and the two side dark current signals are recorded for each high power pulse, and the traces of the power reflection are checked to confirm that the accelerator structure is operating on resonance. The forward and reflected rf power are measured by Schottky detector diodes on a directional coupler of 65 dB attenuation. During the high power test, the breakdowns are identified from the downstream as well as the side dark current signals.

In order to measure the side dark current electron energy spectrum, a dc power supply capable of providing bias voltage from -160 to $+160$ V was installed on one of the side dark current monitors. We use a ceramic $0.1\ \mu\text{F}$ capacitor to electrically isolate the oscilloscope from the

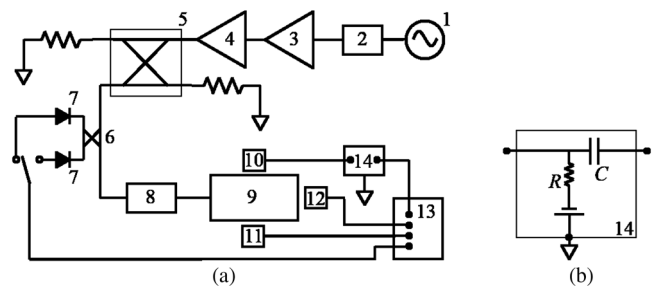


FIG. 1. MIT 17 GHz high power test stand schematic diagram. (a) 1, microwave synthesizer; 2, input pulse modulator; 3, solid state amplifier; 4, 17 GHz klystron; 5, 4.4 dB hybrid; 6, directional coupler; 7, power diodes; 8, TM_{01} mode launcher [31]; 9, structure under test; 10 and 11, side dark current monitors; 12, downstream dark current monitor; 13, digital oscilloscope; 14, dc bias circuit. (b) The dc bias circuit with a 10 k Ω resistor and a 0.1 μF capacitor.

dc bias voltage. With a 10 k Ω resistor, the circuit RC constant is 1 ms, much longer than the 210 ns pulse duration used.

III. DESIGN OF THE STRUCTURE WITH AN ELLIPTICAL SIDEWALL

Figure 2 compares the design of the previously studied single cell standing wave accelerator cavity having a straight sidewall [MIT-DLWG, Fig. 2(a) [32]] with the elliptical sidewall cavity [Fig. 2(b)] discussed in this paper. The single cell straight sidewall cavity was first developed at SLAC [33,34] and later scaled to 17 GHz for testing at MIT. Both designs have a 0.215 aperture-wavelength ratio. In Fig. 2(b), the origin of the ellipse is at the cell center, and the major as well as the minor radii are optimized so that the central cell can have the largest beam shunt impedance, taking into account the transit time effect of an electron traveling at the speed of light. The optimization is based on a single cell CST eigenmode simulation [35], and the central cell with an axisymmetric elliptical profile has an improved shunt impedance of $R_{sh,E} = 70.3$ M Ω /m, compared to $R_{sh,S} = 63.9$ M Ω /m of the MIT-DLWG design.

The normalized field plots are given in Fig. 3 for the structure with elliptical central cell sidewall. The structure operates in a TM_{01} mode (transverse) and π mode (longitudinal). The ratio of the peak on-axis electric field in the input coupling cell, central cell and the output coupling cell is approximately 1 : 2 : 1. The ratio of the peak electric field to the acceleration gradient is 1.86.

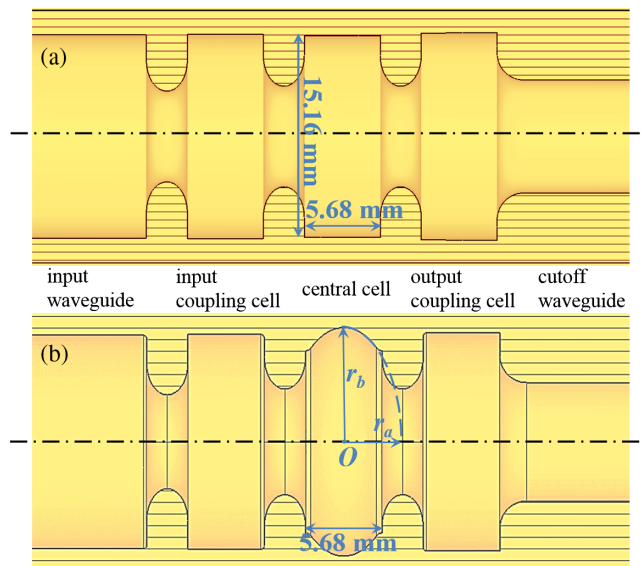


FIG. 2. Axisymmetric view of the 17 GHz single cell standing wave disk-loaded waveguide structure with (a) straight (S) and (b) elliptical (E) central cell sidewall profile (major radius $r_b = 8.16$ mm, minor radius $r_a = 4.30$ mm).

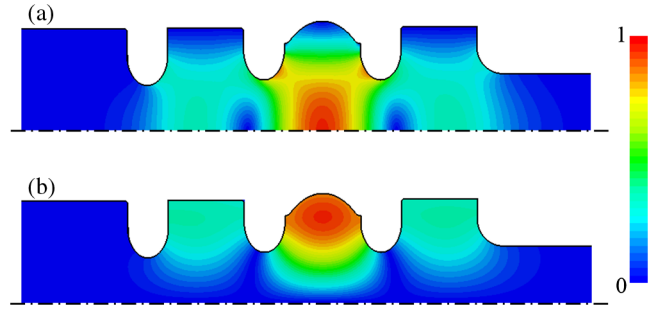


FIG. 3. The π -mode (a) electric and (b) magnetic field distribution of the structure with axisymmetric elliptical central cell sidewall. For a gradient of 100 MV/m, structure surface peak electric and magnetic fields are 186 MV/m and 441 kA/m, and the required input power is 2.1 MW.

IV. INTERNAL DARK CURRENT SIMULATION: MULTIPACTOR MODES

To study the internal dark current generation by electron multipactor on the axisymmetric elliptical central cell sidewall of the E structure, we started from the search for the multipactor modes. We calculated the electron multipactor modes using two different simulation methods, our in-house particle tracking code described in [5] and the particle-in-cell (PIC) simulations in CST PARTICLE STUDIO.

Our in-house particle tracking code calculates the multipactor trajectory formation of different modes on the elliptical cell sidewall. From the calculation, we found the lowest order single surface multipactor modes for one- and two-point multipactors. The sample multipactor trajectories are shown in Fig. 4. The one-point multipactor was designated as the $N = 1$ mode, the trajectory of which takes one rf cycle to complete. The two-point multipactor was defined as the $N = 0.5$ mode, because this multipactor occurs across the accelerator cell sidewall equator ($z = 0$), and it takes half an rf cycle for an electron to travel between two symmetric locations on the two sides of the cell equator.

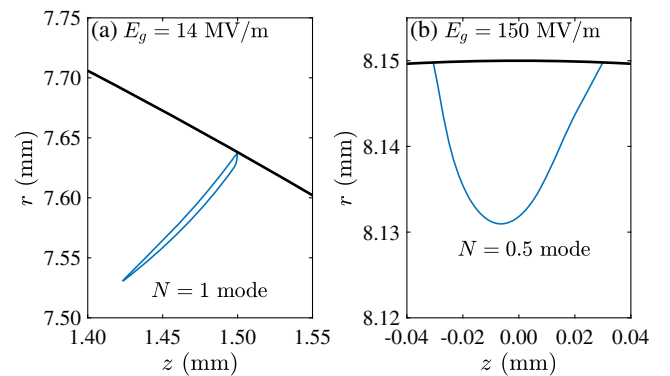


FIG. 4. Sample trajectories of the single surface multipactor modes calculated with our particle tracking code. (a) $N = 1$ mode at the gradient of 14 MV/m, (b) $N = 0.5$ mode at 150 MV/m. $z = 0$ marks the cell equator.

In the code, the secondary electron yield of the multipactor electron colliding on the sidewall surface was also calculated, using Vaughan's model [36,37], with the peak SEY value $\delta_m = 2.1$ for normal incidence at primary electron energy $E_m = 300$ eV, a usual setting used for copper [38,39]. $E_m = 300$ eV is used for all the SEE simulations mentioned in this paper. The simulation results indicated that the $N = 1$ single surface one-point multipactor mode could be excited with SEY above unity over a gradient range of ~ 8 – 35 MV/m on the axisymmetric elliptical sidewall. For $N = 0.5$ mode, the SEY was calculated to be greater than one for acceleration gradient above 150 MV/m.

To verify the calculation results from our in-house code, a series of CST PIC simulations were carried out using the E structure model and the setup shown in Fig. 5, similar to that reported for the straight sidewall structure (S structure) in [5]. On the elliptical sidewall, a strip section with a width of 1.0 mm was assigned with secondary electron emission properties (Vaughan's model). Sampling the internal dark current generated by SEE using such a strip is accurate, since the azimuthal motion of the electrons is not affected by the rf fields [5]. In the simulation, the incident rf power comes in as a square pulse in the TM_{01} mode, the rf fields build up inside the structure, and the electron sources on the iris release electrons upon every rf cycle, each with an average current of $15 \mu\text{A}$. This value was constant and was intentionally chosen to be much less than the field emission current in the real scenario, because the purpose of this simulation was to search for multipactor resonances. Some of the emitted electrons travel to the strip section on the sidewall and generate secondary electrons. If the accelerator cell is susceptible to multipactor, an exponential growth of the internal dark current on the strip will be recorded.

Figure 6 shows the CST predictions of the internal dark current that terminates on the elliptical central cell sidewall plotted against the gradient for two different δ_m values. For the case with $\delta_m = 2.1$, over the gradient range of 0–130 MV/m, no multipactor resonance mode can be identified. This is surprising since the $N = 1$ multipactor

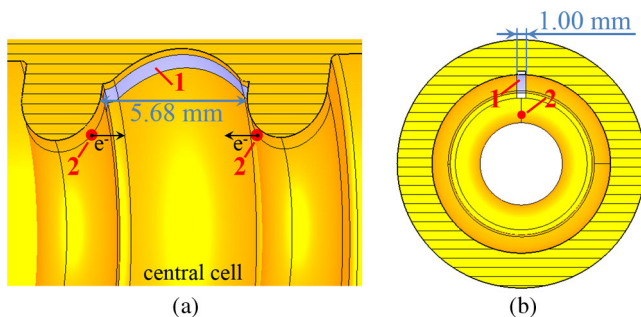


FIG. 5. (a) Longitudinal and (b) transverse cross section views of the PIC simulation model of the structure with axisymmetric elliptical central cell sidewall in CST. 1, the 1.0 mm wide sidewall strip section assigned with SEE properties; 2, the sources of electrons where the peak electric field is located.

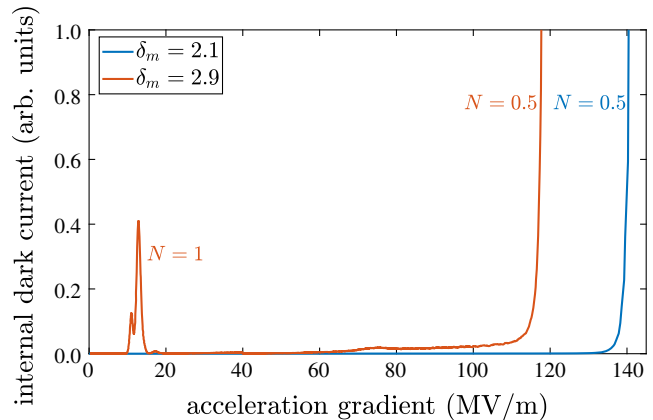


FIG. 6. CST PIC simulation result of the internal dark current intercepted by the axisymmetric elliptical sidewall plotted vs the gradient. A decrease of the δ_m value from 2.9 to 2.1 cancels the $N = 1$ multipactor mode, whereas the $N = 0.5$ mode persists.

mode was clearly seen in the calculation results with our in-house code using the same δ_m value. At a higher gradient, the turn-on of the $N = 0.5$ multipactor mode is identified at around 140 MV/m, in agreement with the result from our in-house code. Since our tests did not reach a gradient of 140 MV/m, we did not expect to see the $N = 0.5$ mode.

Because the $N = 1$ mode was seen in our calculations with our in-house code and in the experiments (described below), we conducted a series of CST calculations by increasing the peak SEY value. The $N = 1$ mode was seen when the value of δ_m reached 2.9, as shown in Fig. 6. The unprocessed copper surface has been reported to present a δ_m value in the range of 1.9–2.5 [38–40]. It is not clear whether the high value of $\delta_m = 2.9$ is a real value for our structure surface or is simply a high value needed to speed up the convergence of the CST code. Using $\delta_m = 2.9$ in CST, the $N = 1$ resonance showed up over a gradient range of 8–16 MV/m (Fig. 6), in agreement with the calculation results using our in-house code. Meanwhile, the threshold gradient for the $N = 0.5$ mode was reduced to around 115 MV/m. In addition, in both cases of the CST PIC simulations, the intensity of the $N = 0.5$ multipactor mode was so strong that the burnthrough of this mode was not achieved. In comparison, the $N = 1$ mode was a minor multipactor mode.

The simulation results for the E structure are a significant improvement over the results for the S structure [5]. In the S structure, both the $N = 1$ and $N = 2$ modes were easily excited in CST simulations with $\delta_m = 2.1$. In the E structure simulations, the $N = 2$ mode is not observed and the $N = 1$ mode is only weakly excited.

V. INTERNAL DARK CURRENT SIMULATION: E STRUCTURE WITH SLITS

In the design of the E structure for the high power experiment, in order to extract the internal dark current

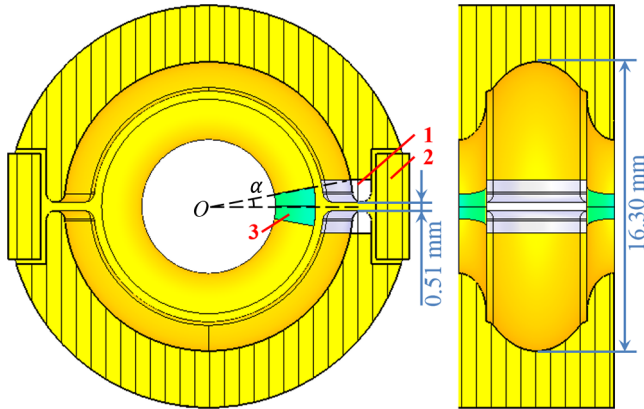


FIG. 7. Central cell design of the experimental E structure with slits opened on the sidewall, as in the CST PIC simulation setup. 1, the sidewall section assigned with SEE properties; 2, the side dark current monitor; 3, field emission area source of electrons.

directly from the central cell, especially from the elliptical sidewall vicinity, two thin slits 0.51 mm wide were opened on the central cell sidewall in parallel with the beam axis, opposite to each other. The experimental E structure was modeled for a CST PIC simulation, as illustrated in Fig. 7. Immediately outside the slits are the side dark current monitors (Faraday cups). These simulations were all carried out with small values of the SEY that are appropriate for the structure after conditioning.

The simulation was conducted at a fixed acceleration gradient of 80 MV/m. Field emission electron sources were assigned on the iris surfaces facing the central cell. The Fowler-Nordheim field emission formula was used with a field enhancement factor of $\beta = 85$ [5], which was derived from our previous experimental result. Some of the field emission electrons from the iris travel to the sidewall and initiate the internal dark current at the sidewall. The opening angle α , defined in Fig. 7, was taken to be $\alpha = 11^\circ$, which was found to be sufficient for the calculation. For these simulations, we assumed the structure was already conditioned and used values of $\delta_m = 1.10, 1.15$ and 1.20 that are typically seen on copper surfaces after electron irradiation [38–40].

At the gradient of 80 MV/m, all the simulations consistently yielded a downstream dark current of 0.46 mA, which was scaled to 7.5 mA assuming that the full range (360°) of both the irises were emitting. When no SEE was used, the side dark current monitor collected only the primary field emission electrons that originated from the irises and traveled through the slit, which contributed to a current of 0.23 mA. With $\delta_m = 1.10, 1.15$ and 1.20 assigned, the side dark current level increased to 0.42, 2.4 and 5.9 mA, respectively. Scaling the internal dark current on the 2α section of the sidewall to that over the entire 360° range, we estimated the total internal dark current interception on the sidewall to be 0.30, 10 and 23 A, for the three δ_m values used. Note that this internal dark

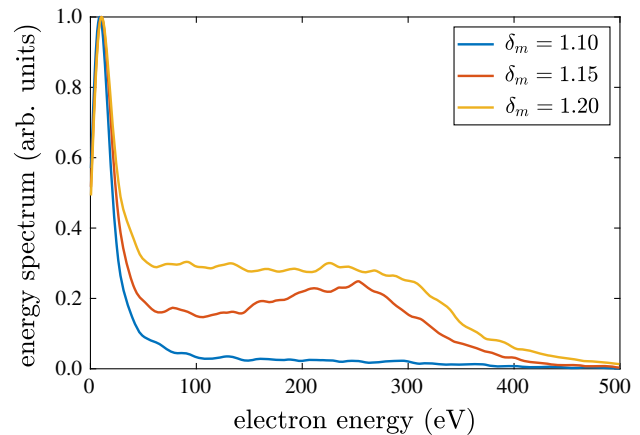


FIG. 8. Side dark current electron energy spectrum calculation results in arbitrary units (arb. units) from CST PIC simulations for $\delta_m = 1.10, 1.15$ and 1.20 assigned to the sidewall section for the SEE properties.

current seen in the simulations was not generated and maintained due to a certain multipactor mode, but to the continuous seeding by field emission from the irises, and it was thus not self-sustaining. These results show that a small improvement in copper surface SEY reduction achieved by rf conditioning can greatly reduce the internal dark current level.

The simulation also used PIC 2-d monitors to record the kinetic energy of each side dark current electron, and the results were used to generate the electron energy spectra for different peak SEY values (δ_m) assigned to the copper sidewall section, as given in Fig. 8 for peak SEY values of $\delta_m = 1.10, 1.15$ and 1.20 . According to the calculation results, the spectrum distribution of the electrons with energy below 30 eV is similar for the different δ_m values used. Over the electron energy range of 50–500 eV, the normalized spectrum is higher for a larger δ_m value assigned. The energy spectrum calculations predict that, as the copper surface SEY decreases during the rf conditioning, the electrons will be more concentrated towards the lower energy range of 0–30 eV.

VI. EXPERIMENTAL E STRUCTURE FABRICATION

The accelerator structure was fabricated using OFHC (oxygen-free high thermal conductivity) copper and built in longitudinal sections as a series of plates, to be clamped by six stainless steel bolts, as illustrated in the assembly drawing in Fig. 9. The side dark current monitors (DC-S1/2) were made of stainless steel, and the downstream dark current monitor (DC-D) was made of OFHC copper. The dark current monitors were installed using ceramic fasteners for electrical insulation. The slit features of the central cell plate were fabricated using wire EDM (electrical discharge machining), and all the other parts were directly machined.

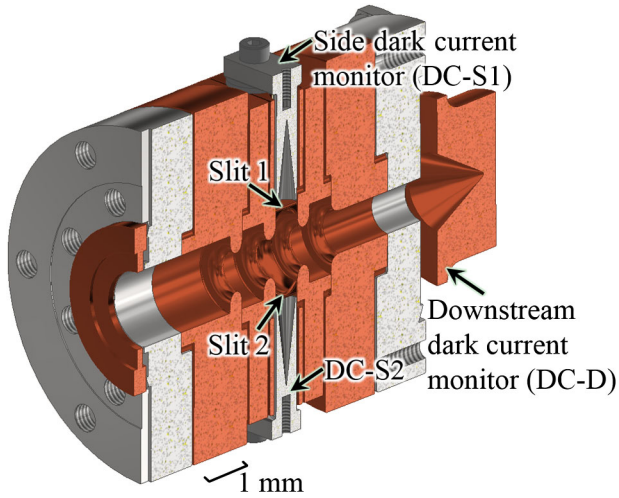


FIG. 9. The half section view of the assembly diagram of the E structure. The two slits are shown in parallel with the cross section. The side dark current monitors receive the current on the immediate outside of the slits.

VII. EXPERIMENTAL RESULTS

A. Cold test

The cold test of the E structure was carried out on a vector network analyzer with a TM_{01} mode launcher [31]. The measured coefficient of reflection in Fig. 10 shows critical coupling of π -mode operation at 17.134 GHz. Table I shows the measured quality factors of the previously studied S structure [5] and the E structure, along with all the other important structure parameters. The value of Q_0 measures the Ohmic power dissipation due to the surface resistance in the accelerator structure, Q_{ext} measures the power loss into the external circuit, and the total (loaded) quality factor Q_l is derived using $Q_l^{-1} = Q_0^{-1} + Q_{\text{ext}}^{-1}$. We also measured the on-axis electric

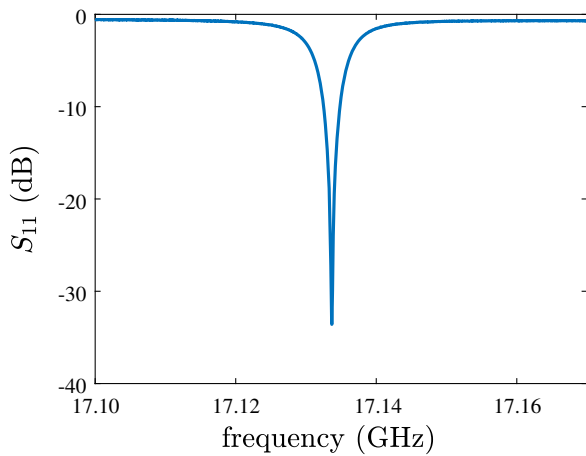


FIG. 10. Reflection coefficient measurement result for the E structure. Critical coupling was achieved for the π mode at 17.134 GHz.

TABLE I. Comparison of the resonant frequency, the quality factors and other important structure parameters between the accelerator structures with axisymmetric straight (S) and elliptical (E) sidewalls.

Structure	S	E
Resonant frequency (GHz)	17.120	17.134
Unloaded quality factor Q_0	5584	5340
External quality factor Q_e	5817	5865
Loaded quality factor Q_l	2849	2795
Gradient (MV/m)	100	100
Microwave power (MW)	2.06	2.10
Peak electric field (MV/m)	198	186
Peak magnetic field (kA/m)	421	441

field distribution of the E structure with the nonresonant perturbation method [41]. A very small dielectric bead was used to perturb the on-axis electric field through the structure, and the result is given in Fig. 11.

B. High power test: Initial conditioning

In the high power test of the E structure, the pulse length of the high power pulses was consistently 210 ns, so that during the final 120 ns of the pulse, the variation of the rf power coupled inside the standing wave accelerator structure was constant to within $\pm 10\%$. In the discussion of the acceleration gradient in this section, we refer to the peak gradient reached in the structure central cell during the rf pulse. The repetition rate of the high power pulse was 1 Hz, and a total of 2.2×10^5 pulses were used in the conditioning of the structure to high gradient. During the conditioning process, we allowed the structure to experience ten consecutive breakdowns before decreasing the rf power to restore the normal operating status of the structure. For the entire high power test, the vacuum chamber pressure was on the scale of 1×10^{-8} Torr.

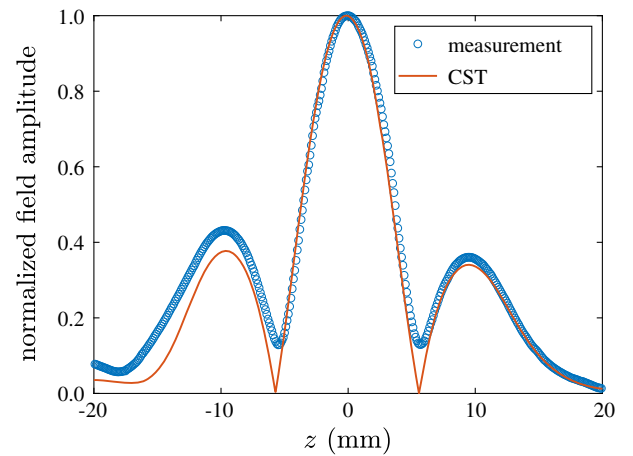


FIG. 11. Measurement result of the on-axis electric field of the E structure compared to the CST MICROWAVE STUDIO simulation result.

The side dark current measurement in the initial stage of the accelerator structure conditioning, i.e., the very first 1×10^4 pulses, revealed in detail how the sidewall surface condition improved. A series of sample traces from this stage of testing is displayed in Fig. 12, from an initial peak gradient of 19 MV/m to a peak gradient of 77 MV/m. At a gradient of 19 MV/m [Fig. 12(a)], the trace of the side dark current is marked with a sharply rising edge when the gradient reaches 14 MV/m. With a small increase of the gradient to 22 MV/m [Fig. 12(b)], the side dark current trace displays two giant current spikes that both have an amplitude of more than 20 mA. These spikes occur at the rising as well as the falling edge of the rf power pulse, peaking consistently at around 14 MV/m gradient. The observed spike feature is inconsistent with field emission theory, which would predict a monotonically increasing current with growing electric field intensity. However, this

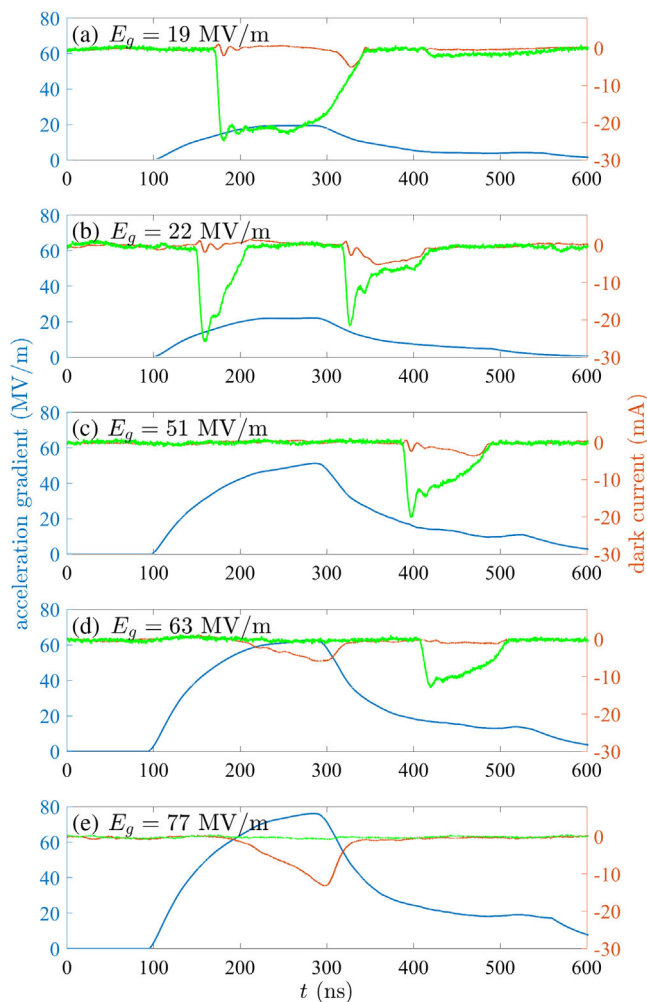


FIG. 12. Sample traces of the gradient (blue), side dark current (green) and downstream dark current (red) measurement results at the very initial stage of the E structure conditioning, for gradients of (a) 19 MV/m, (b) 22 MV/m, (c) 51 MV/m, (d) 63 MV/m and (e) 77 MV/m.

result can be explained by the internal dark current generation from a multipactor process. The measured dependence of the side dark current on the acceleration gradient agrees well with the prediction of the $N = 1$ multipactor mode by our in-house particle tracking code [Fig. 4(a)] as well as the CST PIC simulation (Fig. 6). The appearance of the multipactor is due to the overall high SEY values on the structure inner surfaces at the initial stage of the rf conditioning. As the achievable gradient becomes higher at 51 MV/m [Fig. 12(c)], the multipactor spike on the rising edge of the gradient disappears, because the conditioning is progressing and there is not enough build-up time for the multipactor to develop into a state of intense secondary electron emission. However, there is a small after pulse that follows the main high power microwave pulse, appearing between 300 and 500 ns on the trace. The small power feed from the after pulse causes the decay of the rf fields in the structure to be slower, and multipactor appears over the gradient range of 14 to 20 MV/m in Fig. 12(c), as the gradient decreases. Finally, after about 1×10^4 pulses, the sidewall multipactor has been reduced to about 1 mA at a gradient of 77 MV/m [Fig. 12(e)], and the $N = 1$ mode is not seen thereafter. This result shows that the $N = 1$ multipactor on the sidewall has been effectively eliminated by rf conditioning, indicating a fast initial decrease of the overall surface SEY level.

In the initial conditioning phase, we observed a strong correlation between the downstream and the side dark currents. In Figs. 12(d) and 12(e), the downstream dark current has the expected pulse shape, increasing strongly with increasing gradient. This behavior is consistent with field emission of electrons from the high field region on the irises. However, in Figs. 12(a) and 12(b), the downstream dark current has a shape with small features that are similar and synchronized to the side dark current; the emission vs time is inconsistent with field emission. At low gradients, about 10 to 20 MV/m, the side dark current is dominated by the $N = 1$ multipactor mode, as mentioned above. According to the trajectory calculations of the $N = 1$ mode using the in-house code, multipactor internal dark current can form on the sidewall region close to the iris. Some electrons could travel out to regions of higher electric field and be swept into the downstream dark current. This is the likely explanation for the appearance of the side dark current features in the downstream dark current signal during the initial conditioning phase.

C. High power test: Later conditioning results

After a conditioning period of 2.2×10^5 pulses, over the tested gradient range up to 93 MV/m, the multipactor resonances could no longer be observed. The absence of the sidewall electron multipactor can be seen in Fig. 13, for the accelerator operation at different gradient levels, in comparison with the dark current traces with multipactor features shown in Fig. 12. At the same gradient, the level

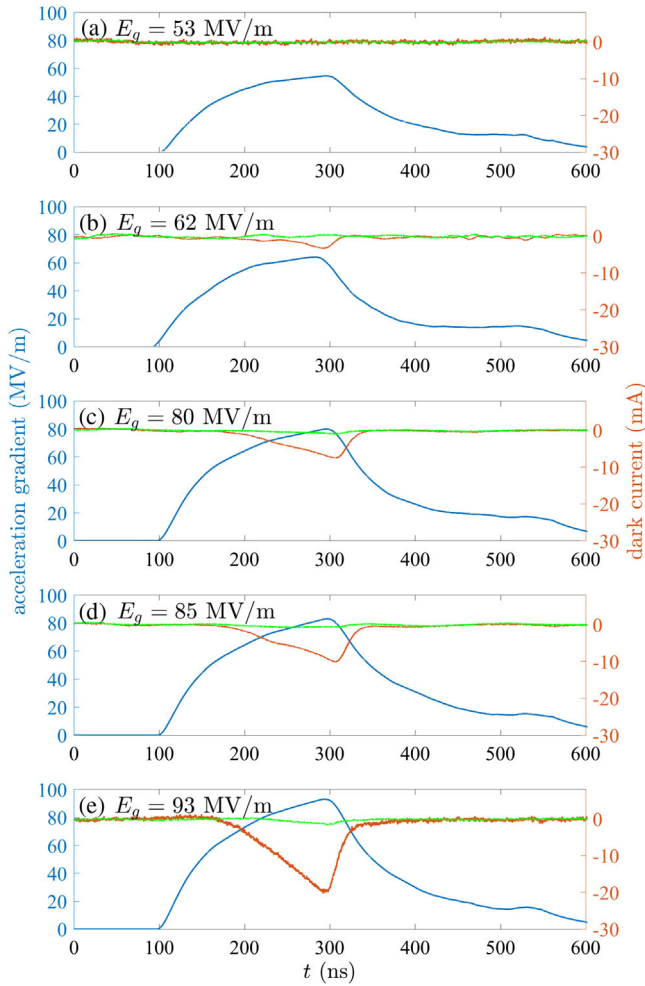


FIG. 13. Sample traces of the gradient (blue), side dark current (green) and downstream dark current (red) measurement results at the finishing stage of the E structure conditioning, for gradients of (a) 53 MV/m, (b) 62 MV/m, (c) 80 MV/m, (d) 85 MV/m and (e) 93 MV/m.

of the downstream dark current was seen to decrease over the rf conditioning period.

The structure achieved a gradient of 93 MV/m [Fig. 13(e)] by the end of the conditioning. At a gradient of 80 MV/m [Fig. 13(c)], the amplitudes of the side and the downstream dark currents were measured to be 0.9 and 7.5 mA. These values are in good agreement with the CST PIC simulation results given in Sec. V, indicating that the copper surface peak SEY has been reduced to a value close to $\delta_m = 1.10$ by rf conditioning. The total amount of the internal dark current interacting with the elliptical sidewall at this gradient was estimated to be 2–3 A.

The total quality factor of the structure was cold tested after the completion of the high power testing. It was found to be equal to or even slightly higher than the value measured prior to testing. There was no visible evidence of damage to the structure.

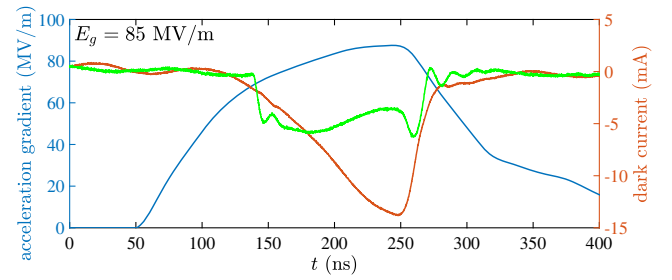


FIG. 14. Sample traces of the gradient (blue), side dark current (green) and downstream dark current (red) measurement results at the finishing stage of the S structure high power test, for a gradient of 85 MV/m [5].

D. Comparison of dark currents in the E and S structures

The high gradient performance of the E structure with an axisymmetric elliptical central cell sidewall can be compared with that of the S structure with an axisymmetric straight central cell sidewall [5], which is shown in Fig. 14 for the case of 85 MV/m gradient, the same gradient level as that in Fig. 13(d). After conditioning to 2.2×10^5 pulses, the downstream dark current is similar for the two structures, but the side dark current is quite different. For the S structure, Fig. 14, the $N = 1$ mode multipactor causes a side dark current of up to 6 mA. In the E structure, the elliptical sidewall design results in a very small (~ 1 mA) side dark current and the elimination of the $N = 1$ and $N = 2$ multipactor modes.

E. Side dark current energy spectrum analysis

To study the energy distribution of the side dark current electrons, we applied a dc bias voltage U_{dc} to one of the side dark current monitors (DC-S1) that was isolated from ground, with a range of -160 V to $+160$ V. The circuit is illustrated in Fig. 1(b).

At different stages of the conditioning (i.e., after a conditioning period of 7.6×10^4 , 1.41×10^5 , and 2.02×10^5 pulses), the amplitude of the side dark current I_s was measured under different U_{dc} values at a fixed acceleration gradient, and the results are shown in Fig. 15.

The results show that, at the limit of $U_{dc} = -160$ V, the amplitude of the side dark current I_s seems to be constant at 0.6 mA for all cases, indicating that the amount of the side dark current with electrons carrying kinetic energy more than 160 eV did not change over the conditioning. It is likely that this portion of the side dark current is not related to the conditioning of the sidewall surface or the sidewall internal dark current generation, and thus should be attributed to the energetic field emission current from the irises.

As the conditioning of the structure proceeded, the gradient of the I_s curve vs U_{dc} near $U_{dc} = 0$ V became progressively greater. This indicated that the energy distribution of the low energy (<160 eV) portion of the side

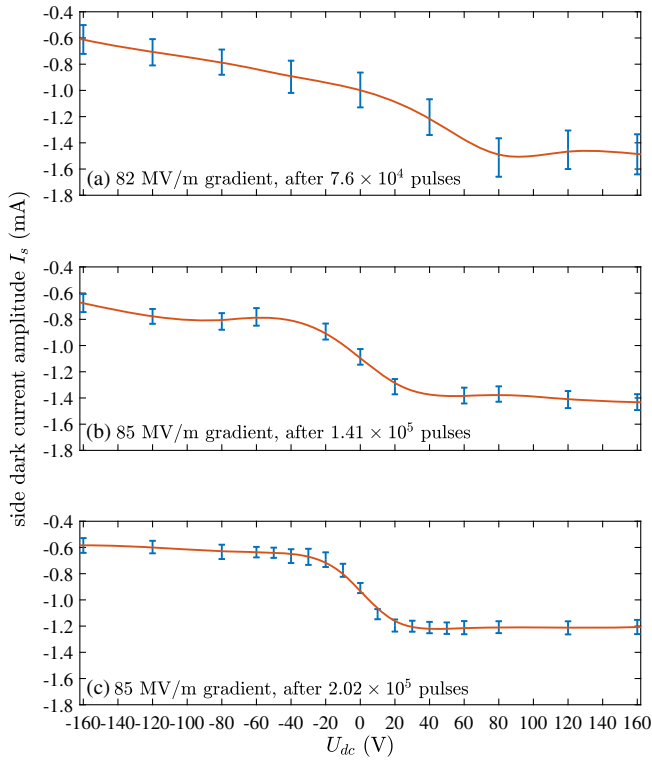


FIG. 15. Measurement results and the spline fitting (visual aid) of the side dark current amplitude under different dc bias voltages applied on the side dark current monitor, (a) after 7.6×10^4 pulses at 82 MV/m gradient; (b) after 1.41×10^5 pulses at 85 MV/m gradient; (c) after 2.02×10^5 pulses at 85 MV/m gradient.

dark current electrons concentrated more towards a lower energy level of 0–30 eV, as the sidewall surface became better conditioned. This is in qualitative agreement with the CST PIC simulation results of the side dark current electron energy spectra shown in Fig. 8 for different surface peak SEY values.

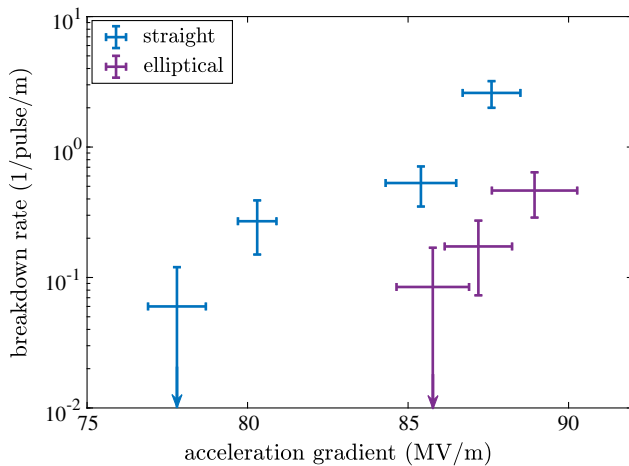


FIG. 16. Breakdown rate measurement results of the accelerator structures with an axisymmetric elliptical (E) and straight (S) central cell sidewall profile.

F. Breakdown rate vs gradient

A comparison of the breakdown rate is shown in Fig. 16 between the E structure and the previously tested S structure. The pulse lengths of the high power pulses used in both the experiments were all 210 ns. The structure with the elliptical sidewall design showed a breakdown rate that was about one decade less than that of the structure with a straight cylindrical central cell design. These breakdown rates would likely be much lower after conditioning to many millions of pulses.

VIII. DISCUSSION AND CONCLUSIONS

A single cell standing wave accelerator structure with an axisymmetric elliptical central cell sidewall was designed for an optimized shunt impedance, fabricated, and tested at high gradient at 17.14 GHz. After conditioning, the electron multipactor modes of $N = 1$ and $N = 2$, previously seen in the accelerator structure with an axisymmetric straight central cell sidewall, were eliminated with the elliptical sidewall design, in good agreement with the CST PIC simulations. The total internal dark current interception on the structure central cell sidewall was measured to be 2–3 A at a gradient of 80 MV/m, an order of magnitude smaller compared to that measured for the S structure with a straight sidewall design. The smaller internal dark current is attributed to the absence of the multipactor modes in the E structure. The downstream dark current of 10 to 15 mA arising from the field emission at the irises was similar in the two structures.

To study the energy spectrum of the side dark current from the E accelerator structure, a varying dc bias voltage was applied on one of the side dark current monitors during the high power test. The result showed that at the end of the rf conditioning period, half of the electrons in the side dark current had kinetic energy less than 160 eV, among which the majority of the electrons had kinetic energy in the range of 0–30 eV. The measured electron energy spectrum agreed with that generated from the CST PIC simulations.

We have presented a unique, detailed experimental study on the internal dark current inside an elliptical sidewall normal conducting cavity. The measurement of the internal dark current confirmed the theoretically predicted suppression of one-point multipactor modes, but also showed a reduced yet significant remaining internal dark current interaction with the elliptical accelerator cell at the equator region. Further approaches for minimizing the internal dark current in an accelerator cavity are still worthy of being investigated.

ACKNOWLEDGMENTS

This work was supported by the Department of Energy High Energy Physics, under Grant No. DE-SC0015566. The authors would like to thank Mr. Ivan Mastovsky for the engineering support in the accelerator laboratory and Dr. Jacob Haimson for very helpful discussions.

- [1] C. K. Ng, N. Folwell, A. Guetz, V. Ivanov, L. Q. Lee, Z. Li, G. Schussman, and K. Ko, Simulating dark current in NLC structures, *Nucl. Instrum. Methods Phys. Res., Sect. A* **558**, 192 (2006).
- [2] K. L. F. Bane, V. A. Dolgashev, T. Raubenheimer, G. V. Stupakov, and J. Wu, Dark currents and their effect on the primary beam in an X-band linac, *Phys. Rev. ST Accel. Beams* **8**, 064401 (2005).
- [3] H. Xu, M. A. Shapiro, and R. J. Temkin, Dark current study of a standing wave disk-loaded waveguide structure at 17 GHz, in *Proceedings of NAPAC'16, Chicago* (JACoW, Geneva, Switzerland, 2016), WEPOB31, pp. 971–973.
- [4] A. Chao, K. H. Mess, M. Tigner, and F. Zimmermann, *Handbook of Accelerator Physics and Engineering* (World Scientific Publishing Co., Singapore, 2013).
- [5] H. Xu, M. A. Shapiro, and R. J. Temkin, Measurements of internal dark current in a 17 GHz, high gradient accelerator structure, *Phys. Rev. Accel. Beams* **22**, 021002 (2019).
- [6] A. G. Mathewson, Vacuum problems in particle accelerators due to interaction of synchrotron radiation, electrons and ions with surfaces, *Vacuum* **44**, 479 (1993).
- [7] D. Menzel and R. Gomer, Desorption from metal surfaces by low-energy electrons, *J. Chem. Phys.* **41**, 3311 (1964).
- [8] C. Wang, L.-H. Chang, M.-H. Chang, L.-J. Chen, F.-T. Chung, M.-C. Lin, Z.-K. Liu, C.-H. Lo, C.-L. Tsai, M.-S. Yeh, and T.-C. Yu, Mitigation of multipacting, enhanced by gas condensation on the high power input coupler of a superconducting rf module, by comprehensive warm aging, *Nucl. Instrum. Methods Phys. Res., Sect. A* **872**, 150 (2017).
- [9] J. Gómez-Goñi and A. G. Mathewson, Temperature dependence of the electron induced gas desorption yields on stainless steel, copper and aluminum, *J. Vac. Sci. Technol.* **15**, 3093 (1997).
- [10] R. Udiljak, D. Anderson, M. Lisak, V. E. Semenov, and J. Puech, Improved model for multipactor in low pressure gas, *Phys. Plasmas* **11**, 5022 (2004).
- [11] J. P. Verboncoeur, H. C. Kim, Y. Chen, and Y. Y. Lau, Modeling rf window breakdown: From vacuum multipactor to volumetric ionization discharge, in *Conference Record of the 2006 Twenty-Seventh International Power Modulator Symposium, Arlington, VA, 2006* (IEEE, Piscataway, NJ, 2006), pp. 13–16.
- [12] M. P. Klyan, V. A. Kritskiĭ, Yu. A. Kulyupin, Yu. N. Kucherenko, K. N. Pilipchak, and S. S. Pop, Electron-bombardment-induced photon emission from copper, *Sov. Phys. JETP* **59**, 3 (1984).
- [13] O. M. Artamonov, S. N. Samarin, and I. I. Yakovlev, Energy threshold characteristics of electron-induced photon emission from Ag, *Radiat. Eff. Defects Solids* **114**, 191 (1990).
- [14] J. H. Coombs, J. K. Gimzewski, B. Reihl, J. K. Sass, and R. R. Schlittler, Photon emission experiments with the scanning tunneling microscope, *J. Microsc.* **152**, 325 (1988).
- [15] V. Baglin, I. R. Collins, J. Gómez-Goñi, O. Gröbner, B. Henrist, N. Hilleret, J.-M. Laurent, M. Pivi, R. Cimino, V. V. Anashin, R. V. Dostovalov, N. V. Fedorov, A. A. Krasnov, O. B. Malyshev, and E. E. Pyata, Experimental investigations of the electron cloud key parameters, CERN Report No. LHC-Project-Report-313, 1999.
- [16] A. F. Leontowich and A. P. Hitchcock, Secondary electron deposition mechanism of carbon contamination, *J. Vac. Sci. Technol. B* **30**, 030601 (2012).
- [17] G. Bienvenu, P. Fernandes, and R. Parodi, An investigation on the field emitted electrons in travelling wave accelerating structures, *Nucl. Instrum. Methods Phys. Res., Sect. A* **320**, 1 (1992).
- [18] F. L. Krawczyk, Status of multipacting simulation capabilities for SCRF applications, Los Alamos National Laboratory, Report No. LA-UR-01-6447, 2001.
- [19] H. Padamsee, Design topics for superconducting rf cavities and ancillaries, CERN Yellow Report No. CERN-2014-005, 2013.
- [20] J. Knobloch, W. Hartung, and H. Padamsee, Multipacting in 1.5-GHz superconducting niobium cavities of the CEBAF shape, in *Proceedings of the 1997 Workshop on RF Superconductivity, Abano Terme, Italy* (INFN, Legnaro, Italy, 1997), SRF97D23, pp. 1017–1027.
- [21] R. L. Geng, Multipacting simulations for superconducting cavities and rf coupler waveguides, in *Proceedings of PAC'03, Portland, OR, 2003* (IEEE, Piscataway, NJ, 2003), pp. 264–268.
- [22] M. A. Gusarova, V. I. Kaminsky, L. V. Kravchuk, S. V. Kutsaev, M. V. Lalayan, N. P. Sobenin, and S. G. Tarasov, Multipacting simulation in accelerating rf structures, *Nucl. Instrum. Methods Phys. Res., Sect. A* **599**, 100 (2009).
- [23] G. Devanz, Multipactor simulations in superconducting cavities and power couplers, *Phys. Rev. ST Accel. Beams* **4**, 012001 (2001).
- [24] V. Shemelin, One-point multipactor in crossed fields of rf cavities, *Phys. Rev. ST Accel. Beams* **16**, 102003 (2013).
- [25] J. W. Wang, RF properties of periodic accelerating structures for linear colliders, SLAC Report No. SLAC-339, 1989.
- [26] J. W. Wang and G. A. Loew, Field emission and rf breakdown in high-gradient room-temperature linac structures, SLAC Report No. SLAC-PUB-7684, 1997.
- [27] A. D. Cahill and J. B. Rosenzweig, rf losses in a high gradient cryogenic copper cavity, *Phys. Rev. Accel. Beams* **21**, 061301 (2018).
- [28] A. D. Cahill, J. B. Rosenzweig, V. A. Dolgashev, S. G. Tantawi, and S. Weathersby, High gradient experiments with X-band cryogenic copper accelerating cavities, *Phys. Rev. Accel. Beams* **21**, 102002 (2018).
- [29] D. Banon-Caballero, W. Wuensch, K. Szypula, N. Catalan Lasheras, B. Gimeno, and A. Faus-Golfe, Combined field emission and multipactor simulation in high gradient rf accelerating structures, in *Proceedings of IPAC'19, Melbourne, Australia* (JACoW, Geneva, Switzerland, 2019), WEPRB058, pp. 2940–2943.
- [30] J. Haimson and B. Mecklenburg, A 71 dB gain, high efficiency relativistic klystron using a high current linear accelerator traveling wave buncher output structure, *AIP Conf. Proc.* **691**, 34 (2003).
- [31] C. Nantista, S. Tantawi, and V. Dolgashev, Low-field accelerator structure couplers and design techniques, *Phys. Rev. ST Accel. Beams* **7**, 072001 (2004).

- [32] B. J. Munroe, J. X. Zhang, H. Xu, M. A. Shapiro, and R. J. Temkin, Experimental high gradient testing of a 17.1 GHz photonic band-gap accelerator structure, *Phys. Rev. Accel. Beams* **19**, 031301 (2016).
- [33] V. Dolgashev, S. Tantawi, C. Nantista, Y. Higashi, and T. Higo, RF breakdown in normal conducting single-cell structures, in *Proceedings of the 21st Particle Accelerator Conference, Knoxville, TN, 2005* (IEEE, Piscataway, NJ, 2005), pp. 595–599.
- [34] V. Dolgashev, S. Tantawi, Y. Higashi, and B. Spataro, Geometric dependence of radio-frequency breakdown in normal conducting accelerating structures, *Appl. Phys. Lett.* **97**, 171501 (2010).
- [35] CST, <http://www.cst.com>.
- [36] J. R. M. Vaughan, A new formula for secondary emission yield, *IEEETrans. Electron Devices* **36**, 1963 (1989).
- [37] R. Vaughan, Secondary emission formulas, *IEEETrans. Electron Devices* **40**, 830 (1993).
- [38] V. Baglin, J. Bojko, O. Gröbner, B. Henrist, N. Hilleret, C. Scheuerlein, and M. Taborelli, The secondary electron yield of technical materials and its variation with surface treatments, CERN Report No. LHC-Project-Report-433, 2000.
- [39] R. Larciprete, D. R. Grosso, M. Commisso, R. Flammini, and R. Cimino, Secondary electron yield of Cu technical surfaces: Dependence on electron irradiation, *Phys. Rev. ST Accel. Beams* **16**, 011002 (2013).
- [40] R. Valizadeh, O. B. Malyshev, S. Wang, S. A. Zolotovskaya, W. A. Gillespie, and A. Abdolvand, Low secondary electron yield engineered surface for electron cloud mitigation, *Appl. Phys. Lett.* **105**, 231605 (2014).
- [41] C. W. Steele, A nonresonant perturbation theory, *IEEE Trans. Microwave Theory Tech.* **14**, 70 (1966).